

Title Page

Structural basis for inhibition of human autotaxin by four potent compounds with distinct modes of binding

Adam J. Stein, Gretchen Bain, Pat Prodanovich, Angelina M. Santini, Janice Darlington, Nina M.P. Stelzer, Ranjinder S. Sidhu, Jeffrey Schaub, Lance Goulet, Dave Lonergan, Imelda Calderon, Jilly F. Evans and John H. Hutchinson

Cayman Chemical Company, Ann Arbor MI: AJS, NMPS, RSS and JS

PharmAkea, San Diego CA: GB, PP, AMS, JD, LG, DL, IC, JFE and JHH

Running Title Page

Running title: Structural basis for inhibition of human autotaxin

Corresponding author:

Gretchen Bain
12780 El Camino Real, Suite 200
San Diego, CA 92130
Phone: 858-764-3872
email gbain@pharmakea.com

No. of Text Pages: 25
No. of Tables: 2
No. of Figures: 6
No. of References: 35
No. of Words in Abstract: 141
No. of Words in Introduction: 556
No. of Words in Discussion: 1550

Abbreviations:

AA- Arachidonic acid

ATX - autotaxin

BNPP - bis(4-nitrophenyl)phosphate

ENPP – ectonucleotide pyrophosphatase/phosphodiesterase

FS-3 – Doubly-labeled Autotaxin substrate

HA155 – (Z)-(4-((4-((3-(4-fluorobenzyl)-2,4-dioxothiazolidin-5-ylidene)methyl)phenoxy)methyl)phenyl)boronic acid

IC₅₀ – half maximal inhibitory concentration

K_m – substrate concentration at half-maximal velocity

LPA – lysophosphatidic acid

LPC – lysophosphatidylcholine

LysoPLD – lysophospholipase D

NUC - nuclease

PAT-078 – (Z)-4-(2-(6-chloro-1-(4-fluorobenzyl)-1H-indol-3-yl)-1-cyanovinyl)benzoic acid

PAT-347 – 3-((6-chloro-7-fluoro-2-methyl-1-(2-oxo-2-(spiro[cyclopropane-1,3'-indolin]-1'-yl)ethyl)-1H-indol-3-yl)thio)-2-fluorobenzoic acid

PAT-352 – (S)-3-(6-(4-fluorobenzyl)-1,3-dioxo-5,6,11,11a-tetrahydro-1H-imidazo[1',5':1,6]pyrido[3,4-b]indol-2(3H)-yl)propanoic acid

PAT-494 – 6-(4-fluorobenzyl)-5,6,11,11a-tetrahydro-1*H*-imidazo[1',5':1,6]pyrido[3,4-*b*]indole-1,3(2*H*)-dione

PDE – phosphodiesterase

PF-8380 – 3,5-dichlorobenzyl 4-(3-oxo-3-(2-oxo-2,3-dihydrobenzo[d]oxazol-6-yl)propyl)piperazine-1-carboxylate

PPase – pyrophosphatase

SMB – somatomedin B

V_{max} – maximal velocity

ABSTRACT

Autotaxin (ATX) is a secreted enzyme that hydrolyzes lysophosphatidylcholine (LPC) to lysophosphatidic acid (LPA). LPA is a bioactive phospholipid that regulates diverse biological processes including cell proliferation, migration, and survival/apoptosis through the activation of a family of G protein-coupled receptors. The ATX-LPA pathway has been implicated in many pathologic conditions including cancer, fibrosis, inflammation, cholestatic pruritus and pain. Therefore, ATX inhibitors represent an attractive strategy for the development of therapeutics to treat a variety of diseases. Mouse and rat ATX have been crystallized previously with LPA or small molecule inhibitors bound. Here we present the crystal structures of human ATX in complex with four previously unpublished, structurally distinct ATX inhibitors. We demonstrate that the mechanism of inhibition of each compound reflects its unique interactions with human ATX. Our studies may provide a basis for the rational design of novel ATX inhibitors.

INTRODUCTION

Autotaxin (also known as ENPP2) is a ~100-kDa secreted glycoprotein that was originally identified as a tumor cell autocrine motility factor and later shown to be responsible for the lysophospholipase D (lysoPLD) activity in human serum that hydrolyzes lysophosphatidylcholine (LPC) to generate LPA ([Gijsbers et al., 2003](#); [Stracke et al., 1992](#); [Tokumura et al., 2002](#); [Umezu-Goto et al., 2002](#)). ATX homozygote knockout mice are embryonic lethal due to abnormal blood vessel development, but ATX heterozygotes are phenotypically normal with approximately 50% circulating lysophosphatidic acid (LPA) compared with wild-type mice ([Tanaka et al., 2006](#); [van Meeteren et al., 2006](#)). LPA stimulates multiple cell signaling pathways through the activation of at least 6 cell surface G protein-coupled receptors and the ATX-LPA pathway has been implicated in a number of physiological and pathological processes ([Yung et al., 2014](#)). Serum LPA and ATX lysoPLD activity are elevated in many disease settings, including renal cancer ([Su et al., 2013](#)), glioblastoma ([Kishi et al., 2006](#)), follicular lymphoma ([Masuda et al., 2008](#)), liver cirrhosis ([Kondo et al., 2014](#)), primary biliary cirrhosis ([Kremer et al., 2010](#)) and atopic dermatitis ([Shimizu et al., 2014](#)), so it is of great interest to the pharmaceutical and medical community to delineate the therapeutic benefit of LPA receptor antagonism or ATX enzyme inhibition.

ATX is most structurally related to ENPP1 and ENPP3, two other members of the seven-member ectonucleotide pyrophosphatase/phosphodiesterase (ENPP) family, however within this family only ATX exhibits lysoPLD activity ([Stefan et al., 2005](#)). ATX retains pyrophosphatase/phosphodiesterase (PPase/PDE) activities ([Clair et al., 1997](#)) and can cleave artificial substrates like FS-3 and bis(4-nitrophenyl)phosphate (BNPP)

([Ferguson et al., 2006](#)). However, it is unclear if the residual PPase/PDE activities of ATX have any physiological or pathological consequences *in vivo*. There are four ATX isoforms (ATX α , β , γ , and δ) that are derived from differential splicing and ATX β and ATX δ are the major stable circulating isoforms ([Giganti et al., 2008](#); [Hashimoto et al., 2012](#)). ATX has two somatomedin B-like binding (SMB) domains at the amino terminus which are cysteine-rich domains that are known to mediate protein-protein interactions. The SMB2 domain binds to β 1 and β 3 integrins ([Fulkerson et al., 2011](#)), which may provide a mechanism for generating LPA in close proximity to its cognate receptors ([Hausmann et al., 2011](#)). The SMB domains are followed by a central catalytic domain which binds two zinc ions and contains an active site threonine and a N-glycan, all of which are critical for the lysoPLD and PPase/PDE activities of ATX ([Gijsbers et al., 2003](#); [Jansen et al., 2007](#)). The C-terminus contains the nuclease-like (NUC) domain which is catalytically inert. The X-ray crystal structures of mouse (PDB ID 3NKM) ([Nishimasu et al., 2011](#)) and rat (PDB ID 2XR9) ([Hausmann et al., 2011](#)) ATX have been previously described and show that the SMB domains and the NUC domain sandwich the catalytic domain and stabilize it. From these crystal structures it is clear that the catalytic domain includes a hydrophobic lipid-binding pocket, however, a second hydrophobic channel was identified and suggested to function as either an entrance channel for the LPC substrates or as an exit channel for the delivery of LPA to its cognate G protein-coupled receptors (PDB ID 3NKN) ([Nishimasu et al., 2011](#)). Here we describe the crystal structures of human ATX in complex with four potent, previously unpublished inhibitors and correlate the mode of inhibition of these inhibitors with each of their unique ATX binding characteristics.

MATERIALS AND METHODS

Human ATX cloning, mutagenesis, recombinant protein expression and purification for crystallography. The ATX cDNA was obtained from Open Biosystems. ATX (amino acids 36-863) was PCR amplified with a C-terminal octa-histidine tag extension. The amplified ATX-C8His gene was ligated into a pFASTBAC (Life Technologies) donor plasmid previously generated with an N-terminal honeybee melittin (HBM) signal peptide sequence. The resulting pFastBac-HBM-ATX-C8His construct was then used to generate DNA mutations that would result in the incorporation of alanine residues at amino acid positions 54 and 411 instead of the normally occurring asparagine residues. The DNA mutations were introduced using the QuickChange II site directed mutagenesis kit (Agilent technologies) according to the manufacturer's instructions. The following primers were used to introduce the mutations: N54A mutation forward primer 5' GACTCCCCCTGGACCGCCATCTCCGGATCTTG and reverse primer 5' CAAGATCCGGAGATGGCGGTCCAGGGGGAGTC and N411A forward primer 5' CCCCAAAGCCATTATTGCCGCTCTCACGTGTAAAAAACC and reverse primer 5' GGTTTTTTTACACGTGAGAGCGGCAATAATGGCTTTGGGG. The resulting pFastBac-HBM-ATX double mutant (N54A/N411A)-C8His construct was transformed into DH10Bac cells (Life Technologies) and bacmid DNA isolated and used to transfect Sf21 cells. Virus was amplified and used to generate BIIC stocks. Amplified virus or BIIC stocks were used to express mature secreted ATX. Protein expression in media was analyzed by immunoblotting using rabbit anti-ATX polyclonal antibody (Cayman Chemical). After three days, 4-6 liters of media was collected and filtered using a glass pre-filter and 0.45µm filter. Ni-NTA (MC Labs) resin pre-equilibrated with buffer A (50mM Tris pH 8.0, 150mM NaCl, and 25mM imidazole) was incubated with the clarified

media overnight at 4°C. Ni-NTA resin was pelleted by low speed centrifugation and the unbound proteins were removed. The resin was washed with 300 column volumes of buffer A and eluted with buffer B (50 mM Tris pH 8.0, 150 mM NaCl, and 300 mM imidazole). The fractions containing ATX protein were pooled and dialyzed overnight at 4°C in SEC buffer (50 mM Tris pH 8.0, 150 mM NaCl, 5 mM CaCl₂, and 5 mM MgCl₂). The protein was concentrated to 2 mL and loaded on a HiLoad Superdex S-200 16/600 (GE Healthcare) SEC column. Fractions containing monodisperse ATX protein were pooled, concentrated to 11 mg/mL, and flash frozen in liquid nitrogen.

Crystallization and Data Collection.

General crystallization protocol: Complex ATX/inhibitor was made by adding 5 mM inhibitor to 11 mg/mL double mutant ATX. Crystals of ATX/inhibitor were grown at room temperature by sitting-drop vapor diffusion against a reservoir containing 10-20% PEG 3350 (mother liquor) and various salts. Crystals were quickly transferred into a cryo-protectant containing the mother liquid supplemented with 20% glycerol and flash frozen in liquid nitrogen prior to data collection. All data were collected at -160°C at the LS-CAT (21-ID) beamline at Argonne National Laboratory. Data were integrated, scaled, and merged using HKL2000 ([Otwinowski and Minor, 1997](#)).

ATX/PAT-078. With the addition of 0.4 M NaSCN to the mother liquor, cube-like crystals grew to a maximum dimension of 50 x 50 x 100 µm within one week. The best crystals diffracted to 1.8 Å.

ATX/PAT-347. Initial attempts to co-crystallize ATX/PAT-347 failed. As a result, ATX/PAT-078 crystals were cross-seeded into conditions that contained ATX/PAT-347

material. Crystals nucleated in a solution of the mother liquor and 0.2 M NaCl. Cube-like crystals nucleated in two weeks and to a maximum dimension of 75 x 75 x 50 μm within three weeks. The best crystals diffracted to 1.75 \AA .

ATX/PAT-494. With the addition of 0.3 M KSCN to the mother liquor, cube-like crystals grew to a maximum dimension of 50 x 50 x 50 μm within three weeks. The best crystals diffracted to 2.6 \AA .

ATX/PAT-352. With the addition of 4% Tacsimate pH 6.0 to the mother liquor, plate-like crystals grew to a maximum dimension of 100 x 100 x 100 μm within one week. The best crystals diffracted to 2.95 \AA .

Structure determination. All refinement statistics are listed Table 2.

General procedure – Refinement of ATX/inhibitor structures. The structure of an ATX/inhibitor complex was determined by molecular replacement techniques as implemented in PHASER ([McCoy et al., 2007](#)). The solution was refined using rigid body refinement in REFMAC ([Vagin et al., 2004](#)). After rigid body refinement, rounds of manual rebuilding were followed by cycles of torsion-angle dynamics, positional refinement, and individual B-factor refinement using COOT ([Emsley and Cowtan, 2004](#)) and REFMAC. This was all performed in the absence of the inhibitor. After placement of the solvent molecules, the inhibitor was modeled and refined.

ATX/PAT-078. The mouse ATX crystal structure (PDBID: 3WAY) was used as the search model. The solution was refined and inspection of the initial electron density maps showed unambiguous density for PAT-078 in the LPA binding site.

ATX/PAT-352. The ATX/PAT-078 crystal structure without any of the secondary molecules was used as the search model. The solution was refined and the initial electron density maps showed unambiguous density for two molecules of PAT-352 – one partially in the LPA binding site as well as a secondary allosteric site. Further refinement was performed as described for ATX/PAT-078.

ATX/PAT-347 and ATX/PAT-494. The structures of both ATX/PAT-347 and ATX/PAT-494 were determined as described for the ATX/PAT-352 structure. The electron density for PAT-347 and 14:0 LPA are shown in Supplementary Figure 1 along with the electron density of PAT-494 and AA molecules are shown in Supplementary Figure 2.

Coordinates and structure factor amplitudes were deposited to the Protein Data Bank using the accession codes 4ZG6 (PAT-078), 4ZG7 (PAT-347), 4ZGA (PAT-494), and 4ZG9 (PAT-352).

Compound synthesis

PAT-352: (S)-3-(6-(4-fluorobenzyl)-1,3-dioxo-5,6,11,11a-tetrahydro-1H-imidazo[1',5':1,6]pyrido[3,4-b]indol-2(3H)-yl)propanoic acid. Prepared as described in patent application WO2015/077502, Example 5, compound 1-5.

PAT-494: 6-(4-fluorobenzyl)-5,6,11,11a-tetrahydro-1H-imidazo[1',5':1,6]pyrido[3,4-b]indole-1,3(2H)-dione. Prepared as described in patent application WO2015/077502, Example 14.

PAT-347: 3-((6-chloro-7-fluoro-2-methyl-1-(2-oxo-2-(spiro[cyclopropane-1,3'-indolin]-1'-yl)ethyl)-1H-indol-3-yl)thio)-2-fluorobenzoic acid. Prepared as described in patent application WO2015/048301, Example 71.

PAT-078: (Z)-4-(2-(6-chloro-1-(4-fluorobenzyl)-1H-indol-3-yl)-1-cyanovinyl)benzoic acid. Prepared as described in patent application WO2015/042953, Example 1.

Protein production for ATX isoforms. Each of the four ATX isoforms was cloned by standard PCR techniques into the XbaI/BamHI sites of pcDNA3.1(-) using the following primer pair: forward primer 5' TCTAGACCACCATGGCAAGGAGGAGCTCGTTCC and reverse primer 5' GGATCCTTAAATCTCGCTCTCATATGTATGC. ATX α and δ were cloned from human skeletal muscle cDNA, human ATX β was cloned from human kidney cDNA and human ATX γ was cloned from human brain cDNA. All cDNAs were verified by sequence analysis. For production of ATX protein, 293T/17 [HEK-293T/17] (ATCC[®] CRL-11268) cells were transiently transfected with each expression construct using Lipofectamine 2000 (Life Technologies) according to the manufacturer's instructions. Cells were plated one day prior to transfection and seven hours after transfection, media was removed and the cells washed once with PBS before the addition of serum-free, phenol-red free media. Cells were incubated for an additional 48 hours at 37°C and 5% CO₂ before the conditioned media was collected, centrifuged to remove cells and debris and frozen at -80°C. Concentrated conditioned medium from Hep 3B2.1-7 [Hep 3B, Hep-3B, Hep3B] (ATCC[®] HB-8064) cells was generated by culturing the cells in growth media until ~80% confluence. The cells were then washed once with PBS before the addition of serum-free, phenol-red free growth media. Cells were incubated for an additional 48 hours at 37°C and 5% CO₂ before the conditioned

media was collected and centrifuged to remove cells and debris. The conditioned media was concentrated 10-20X using 30K MWCO Centriprep centrifugal filters (Millipore) according to the manufacturer's instructions.

LysoPLD activity assay. ATX lysoPLD activity was measured by the release of choline from the substrate, 14:0 LPC. Briefly, conditioned medium from transiently transfected 293T/17 [HEK-293T/17] (ATCC[®] CRL-11268) cells or concentrated conditioned medium from Hep 3B2.1-7 [Hep 3B, Hep-3B, Hep3B] (ATCC[®] HB-8064) cells was incubated with inhibitor (or LPA, AA or vehicle control) in lysoPLD buffer (100 mM Tris, pH9, 500 mM NaCl, 5 mM MgCl₂, 5 mM CaCl₂ and 0.05% triton X-100) for 15 min at 37°C before the addition of 14:0 LPC to 100 μM. After an additional 1.5 hr incubation at 37°C, the liberated choline was detected by the addition of an equal volume of TOOS detection reagent (4.5 mM 4-aminoantioyrine, 2.7 mM N-ethyl-N-(2-hydroxy-3-sulfopropyl)-m-toluidine, 20 units mL⁻¹ horseradish peroxidase and 3 units mL⁻¹ choline oxidase in 50 mM Tris pH8, 4.5 mM MgCl₂) and a further incubation for 10 min at room temperature. Color development was detected using a Molecular Devices SpectraMax Plus by measuring the absorbance at a wavelength of 555 nm. The concentration of choline was calculated from a standard curve generated using choline chloride. The ATX compounds were tested for inhibition of the choline oxidase and horse-radish peroxidase enzymes using a choline standard curve and shown to have no inhibition of these enzymes at concentrations that showed 100% inhibition in the LysoPLD assay (1 μM inhibitor) (data not shown).

BNPP cleavage assay. The ability of ATX to cleave the nucleotide-like substrate *bis*-(*p*-nitrophenyl) phosphate (BNPP) was determined by measuring the generation of the

yellow product, *p*-nitrophenyl. Briefly, conditioned medium from 293T/17 [HEK-293T/17] (ATCC[®] CRL-11268) cells transiently transfected with human ATX β was incubated with inhibitor (or LPA, AA or vehicle control) in assay buffer (50 mM Tris, pH8, 140 mM NaCl, 1 mM MgCl₂, 1 mM CaCl₂ and 5 mM KCl) for 15 min at 37°C before the addition of BNPP to 1.5 mM. After an additional 1-3hr incubation at 37°C, the liberated *p*-nitrophenyl was detected using a Molecular Devices SpectraMax Plus by measuring the absorbance at 405 nm.

FS-3 cleavage assay. The ability of ATX to cleave FS-3 was determined fluorometrically. Briefly, conditioned medium from 293T/17 [HEK-293T/17] (ATCC[®] CRL-11268) cells transiently transfected with human ATX β was incubated with inhibitor (or LPA, AA or vehicle control) in Assay buffer (50 mM Tris, pH8, 140 mM NaCl, 1 mM MgCl₂, 1 mM CaCl₂ and 5 mM KCl) for 15 min at 37°C before the addition of FS-3 to 2.5 μ M. After an additional ~1hr incubation at 37°C, fluorescence was measured using a Molecular Devices FlexStation 3 at excitation = 485 nm and emission = 528 nm.

Enzyme kinetics. The lysoPLD assay was used to evaluate enzyme kinetics in the presence of each inhibitor. Briefly, conditioned medium from 293T/17 [HEK-293T/17] (ATCC[®] CRL-11268) cells transiently transfected with human ATX β was incubated with varying concentrations of 14:0 LPC in the absence or presence of inhibitor (0.5X-4X the IC₅₀ value determined from concentration response curves) in lysoPLD buffer for 1.5h at 37°C before the addition of the color reagents for detection of released choline. The data were plotted and substrate/velocity curves generated using GraphPad Prism 6. K_m

and V_{\max} values were generated in GraphPad Prism 6 from nonlinear regression analysis of the Michaelis-Menten data.

Western blotting. ATX expression in conditioned media was evaluated by Western blotting using an affinity-purified polyclonal goat IgG against human ATX (R&D Systems Cat# AF5255). Briefly, conditioned medium from 293T/17 [HEK-293T/17] (ATCC[®] CRL-11268) cells transiently transfected with ATX α , β , γ or δ or concentrated conditioned medium from Hep 3B2.1-7 [Hep 3B, Hep-3B, Hep3B] (ATCC[®] HB-8064) cells was separated on Bolt[®] 4-12% Bis-Tris protein gels and then transferred to nitrocellulose using the iBlot[®] gel transfer device (Life Technologies). Blots were incubated with the anti-ATX antibody (1:250 dilution) for 2hr at room temperature before incubation with an IRDye conjugated anti-goat secondary antibody and imaging with an Odyssey CLx (LI-COR Biosciences).

Human blood lysoPLD assay. The lysoPLD activity of ATX in human blood was evaluated by measuring the generation of 20:4 LPA from endogenous LPC. Blood was collected from consenting human volunteers into heparin vacutainer tubes and used within 1hr of draw. Prior to setting up the assay, an aliquot of blood was removed, centrifuged at 800 x g for 10 min at 4°C to isolate plasma and the plasma used for the determination of baseline 20:4 LPA concentrations. To assay for ATX activity, 200 μ L of blood was incubated with inhibitor (or DMSO vehicle control) for 4hr at 37°C. After the incubation, the blood was centrifuged as above to isolate plasma and 40 μ L of the plasma processed for the determination of 20:4 LPA concentrations by LC-MS. The plasma was processed by the addition of 5 volumes of ice-cold methanol containing 125 ng/mL 17:0 LPA as an internal standard and incubation at -20 °C for 10 min before

centrifuging at 4000 x g for 10 min at 4 °C. 150 µL of the supernatant was transferred to a 96-well plate and diluted with 100 µL of an organic solution (90:10:0.1 of water/acetonitrile/ammonium hydroxide) for analysis of 20:4 LPA concentrations by LC-MS. LPA 20:4 and the internal standard (LPA 17:0) were analyzed on a quadrupole mass spectrometer (ABI Sciex 4000QTrap) in the negative ion mode (ESI) by multiple reaction monitoring (MRM). The mobile phases contain 0.1% ammonium hydroxide in 90% water/10% acetonitrile (solvent A) and 0.1% ammonium hydroxide in 90% acetonitrile/10% water (solvent B). The flow rate was maintained at 0.8 mL/min and the total run time was 3 min. Analytes were separated using a linear gradient as follows: 1) mobile phase was held for 0.5 min at 10% B; 2) B was increased from 10% to 90% over the next 1 min; 3) B was held constant for 0.5 min at 90%; and 4) B was returned to the initial gradient conditions.

RESULTS

The structure and inhibition of human autotaxin

A variant of full-length human ATX (residues 36-863, β -isoform) was generated in which the asparagine glycosylation sites at amino acid positions 54 and 411 were mutated to alanines (N54A and N411A) (Fig. 1A) ([Hausmann et al., 2011](#)). The two glycosylation sites were mutated to potentially enhance crystal formation. This double-deglycosylation mutant ATX was expressed in Sf21 insect cells, purified and found to be appropriately reduced in molecular weight and with reduced catalytic activity compared to the wild-type protein (Supplementary Fig. 3A, B) ([Pradere et al., 2007](#)). X-ray data from human ATX co-crystallized with four potent ATX inhibitors derived from internal research at PharmAkea (Fig. 2A) were obtained at various resolutions by molecular replacement as described in Online Methods. The data collection and crystal refinement details for each of the four structures are outlined in Table 1. The human ATX sequence is >90% identical to rodent sequences ([Sievers et al., 2011](#)) and the domain organization and overall structure shows high homology to the previously crystallized mouse (PDB ID 3NKM) ([Nishimasu et al., 2011](#)) and rat (PDB ID 2XR9) ([Hausmann et al., 2011](#)) ATX enzymes (Fig. 1B).

The potencies of two published ATX inhibitors, HA155 ([Albers et al., 2010](#)) and PF-8380 ([Gierse et al., 2010](#)), and four previously unpublished ATX inhibitors (PAT-078, PAT-347, PAT-494 and PAT-352) (Fig. 2A) were determined against distinct enzymatic activities of ATX, including the lysoPLD and PPase/PDE activities by employing diverse substrates, including LPC, FS-3 and BNPP (Fig. 2B). Additionally, the potencies of these inhibitors against the lysoPLD activity of the four different ATX isoforms (α , β , γ , δ)

was evaluated using conditioned medium from HEK293 cells recombinantly expressing each isoform (Supplementary Fig. 4A-E). Potencies against the lysoPLD activity of endogenous ATX were evaluated using concentrated conditioned media from Hep3B human hepatocellular carcinoma cells and human blood. LysoPLD activity assays were carried out using C_{14:0} acyl chain LPC since this was shown by optimization studies to be a preferred substrate species *in vitro* ([Giganti et al., 2008](#)). All six compounds tested inhibited the lysoPLD activity of human ATX β maximally, albeit with IC₅₀ values that ranged from 0.002-0.472 μ M (Table 2 and Fig. 2C) and each was equipotent at inhibiting the lysoPLD activity of the four ATX isoforms (Supplementary Fig. 4C-E, Supplementary Table 1). All six test compounds maximally inhibited lysoPLD activity of endogenous ATX from human Hep3B cells and human blood, with rank order potencies similar to the recombinant ATX inhibition (Supplementary Fig. 5A, B and Supplementary Table 1). Interestingly, the six compounds varied in their ability to inhibit cleavage of the artificial substrates, BNPP and FS-3. HA155 and PF-8380 showed maximal 100% inhibition of BNPP cleavage with average IC₅₀ values of 0.007 μ M and 0.001 μ M, respectively (Fig. 2D and Table 2), whereas three of the PAT compounds (PAT-347, -352 and -494) inhibited BNPP cleavage at only ~50-75% of maximum, but with similar IC₅₀ values to HA155 and PF-8380 (0.003-0.006 μ M) (Fig. 2D and Table 2). PAT-078 was a very poor inhibitor of BNPP hydrolysis showing a maximum inhibition of only ~15% (Fig. 2D and Table 2). HA155, PF-8380, and two of the PAT compounds (PAT-078 and PAT-352) showed potent, approximately maximal inhibition of FS-3 cleavage with average IC₅₀ values ranging from 0.0004-0.011 μ M (Fig. 2E and Table 2), however,

PAT-347 and PAT-494 were unable to inhibit the ATX-mediated cleavage of FS-3 (Fig. 2E and Table 2).

The mode of enzyme inhibition for lysoPLD activity was evaluated for each PAT compound by generating substrate/velocity curves in the presence of varying concentrations of inhibitor and determining the effects on K_m and V_{max} (Fig. 3). Increasing concentrations of PAT-078 resulted in a linear increase in K_m , very little change in V_{max} and a large alpha value ($\alpha=52$), a profile characteristic of a competitive inhibitor (Fig. 3A, B). Increasing concentrations of PAT-347, PAT-494 or PAT-352 resulted in curvilinear increases in K_m and curvilinear decreases in V_{max} which are consistent with a non-competitive mode of inhibition. PAT-347 had an alpha value close to 1 (Fig. 3C, D), consistent with a true non-competitive mode of inhibition, whereas PAT-352 and PAT-494 displayed higher alpha values which are more consistent with a mixed-mode of inhibition (Fig. 3E-H).

Crystal structure of ATX bound to the competitive inhibitor PAT-078

The crystal structure of human ATX solved with PAT-078 bound (PDB ID 4ZG6) showed that this inhibitor binds in the catalytic site and partially fills the substrate and LPA/HA155 binding site (Fig. 4A) ([Hausmann et al., 2011](#); [Nishimasu et al., 2011](#)). Two polar contacts exist between PAT-078 and ATX. The more important of the two contacts is the PAT-078 vinyl-nitrile-backbone coordination of Phe275 (3.1Å). The other contact is a water-mediated interaction with the PAT-078 benzoic acid (3.2Å) (Fig. 4A). Other key interactions include π -stacking between the vinyl indole and Tyr307 with the fluoro-phenyl group tightly packed into a pocket aligned with Leu217 and Ala218 (Fig. 4A).

Leu214 complements the vinyl indole-Tyr307 interaction by packing against the chloro-indole of PAT-078 (Fig. 4A). The carboxylic acid points toward the solvent and does not interact with the zinc. This is in contrast to the HA155 crystal structure in which the boronic acid interacts with both zinc atoms and the active site Thr210 (Thr209 in rat) (PDB ID 2XRG) ([Hausmann et al., 2011](#)) (Fig 4B).

Crystal structure of ATX bound to the non-competitive inhibitor PAT-347

The crystal structure of ATX with PAT-347 bound (PDB ID 4ZG7) showed that it co-crystallized with an endogenous C_{14:0} acyl chain LPA (14:0 LPA) (Fig. 4C). In the enzyme kinetic analysis, PAT-347 displayed a non-competitive mode of inhibition with respect to the lysoPLD activity and in the crystal structure it binds in an allosteric site adjacent to the catalytic site (Fig. 4C). This non-competitive site is the same as the previously reported putative secondary LPA-binding site in the mouse ATX crystal structure, and has also been identified as a hydrophobic channel ([Nishimasu et al., 2011](#)). The 14:0 LPA binds in the catalytic site in a similar fashion to the 14:0 LPA bound in the mouse ATX crystal structure (PDB ID 3NKN) ([Nishimasu et al., 2011](#)). The PAT-347 indole forms a π - π -interaction with Phe275 (edge:face) with another π - π -interaction between His252 and the cyclopropyl-dihydroindole (face:face) (Fig. 4C). The PAT-347 benzoic acid makes polar contacts with a glycerol molecule added during the crystal cryo-protection process and is oriented toward the solvent boundary. Similarly, Phe250 introduces an edge on π - π -interaction with the benzoic acid (Fig. 4C). When the crystal structures of PAT-347/LPA are overlaid with PAT-078, competitive vs. non-competitive binding sites are easily distinguishable (Fig. 4D). Although LPA has been published to inhibit ATX activity ([van Meeteren et al., 2005](#)), we tested three different species of LPA

(14:0, 18:1 or 20:4) and found that none of these LPA molecules has any effect on the lysoPLD activity of ATX (Supplementary Fig. 6A and data not shown). However, all three species of LPA tested inhibited the ATX mediated cleavage of BNPP and FS-3 (Supplementary Fig. 6B, C and data not shown).

Crystal structure of ATX bound to the mixed-mode inhibitor PAT-494

Crystallization with PAT-494 identified one molecule of PAT-494 and unexpectedly, one molecule of arachidonic acid (AA) each bound in a distinct site outside the catalytic site (PDB ID 4ZGA) (Fig. 5A). AA was not added during the crystallization process so the enzyme must have selected this molecule from the Sf21 insect fatty-acid pools. Racemic PAT-494 was used in the crystallization process, however, it is clear from the X-ray structure that the enzyme has selected the more potent 'S'-enantiomer (approximately 2-fold more potent than the racemic compound) (data not shown). The phenyl ring of the tetracyclic core of PAT-494 is aligned in a pocket formed by Phe211, Leu214 and Tyr215 (Fig. 5A). A second pocket consisting of Ser170, Leu217 and Phe274 surrounds the fluoro-phenyl group in a distant edge-face interaction. The hydantoin of PAT-494 π -stacks with Tyr307 and one of the carbonyls makes an H-bond with the Phe275 amide, analogous to the PAT-078 cyano-amide bond (Fig. 5A). An overlay of the competitive inhibitor PAT-078 and the mixed-mode inhibitor PAT-494 (with AA co-crystallized) clearly shows that these two compounds occupy distinct, but partially overlapping binding sites (Fig. 5B). Additionally, this overlay shows that the carboxylic acid of PAT-078 occupies similar space as the acid in AA, which would preclude AA from binding with PAT-078 (Fig. 5B). An overlay of the non-competitive inhibitor PAT-347 and the mixed-mode inhibitor PAT-494 (with AA co-

crystallized) shows that there is considerable overlap between the arachidonic acid binding site and the PAT-347 allosteric binding site within the hydrophobic channel (Fig. 5C). A surface representation of both the LPA binding site identified in the PAT-347 crystal and the AA binding site identified in the PAT-494 crystal clearly show that these are two distinct binding regions (Fig. 5D). Although AA clearly binds to the enzyme in the PAT-494 crystal, when incubated with the enzyme alone, it is unable to inhibit the lysoPLD activity of ATX (Supplementary Fig. 7A) or inhibit the cleavage of BNPP (Supplementary Fig. 7B) at concentrations up to 100 μ M. However, AA does inhibit the ATX-mediated cleavage of FS-3 with an average IC_{50} value of 4.5 μ M (Supplementary Fig. 7C).

Crystal structure of ATX bound to the mixed-mode inhibitor PAT-352

Unexpectedly, the PAT-352 crystal structure showed a novel binding mode wherein two molecules of PAT-352 bound to the enzyme (PDB ID 4ZG9). One molecule of PAT-352 binds partially in the competitive site (site 1), analogous to PAT-494, and a second molecule binds in a secondary site adjacent to the competitive site (site 2) (Fig. 6A). The binding of PAT-352 in the secondary binding site is the result of a significant re-arrangement in loop 240-255 (Fig. 6B,C). The newly folded loop extends into the catalytic site where Arg247 hydrogen bonds to the PAT-352 carboxylic acid at the entrance to the hydrophobic pocket. As a result, the loop occludes the allosteric site occupied by PAT-347 and arachidonic acid (Fig. 6B,C). Interestingly, the carboxylic acid of PAT-352 (site 1) binds in a region distinct from where the acids of PAT-078, PAT-347 and AA are co-located. In the PAT-352 secondary site, Trp254 from below π -stacks with the indole ring of PAT-352 while the fluoro-phenyl ring is sandwiched between Arg440,

Met233, and Phe242 from above (Fig. 6C). As shown in Figure 6D, the overlay of all four crystal structures shows the distinct binding mode of each inhibitor as well as the co-crystallized 14:0 LPA and arachidonic acid molecules. The ATX structure shown as a semi-transparent surface highlights the major structural domains, including the hydrophobic pocket which extends from the active site and the distinct allosteric/arachidonic acid binding site identified by the hydrophobic channel (Fig. 6E). The approximate volumes of 14:0 LPA bound in the hydrophobic pocket and arachidonic acid bound in the hydrophobic channel are depicted in Figure 6F.

DISCUSSION

The overall domain architecture of human ATX is very similar to that of the mouse (PDB ID 3NKM) ([Nishimasu et al., 2011](#)) and rat (PDB ID 2XR9) ([Hausmann et al., 2011](#)) enzymes. The binding of four potent, previously unpublished inhibitors synthesized at PharmAkea were characterized in this study. These inhibitors represent three different structural classes (PAT-494 and PAT-352 are structurally related) and show some structural similarities. They all contain an indole ring with a phenyl containing indole N-substituent. Three of the inhibitors contain a carboxylic acid, whereas PAT-494 has an acidic hydantoin group. Additionally, all compounds have the acidic group extending from the C-3 position of the indole, and potently inhibit the lysoPLD activity of ATX. However, despite these structural similarities, we noted significant differences in the mechanism of inhibition of the lysoPLD activity and differences in the abilities of these compounds to inhibit cleavage of the artificial substrates, FS-3 and BNPP.

PAT-078 is bound deep in the hydrophobic pocket of the competitive site, partially occluding the LPA and presumed LPC binding site. This binding would prevent substrate access which is fully consistent with the competitive mode of inhibition. However, unlike the competitive inhibitor HA155, which coordinates to zinc (PDB ID 2XRG), PAT-078 does not extend far enough to interact with the active site zincs, and thus is unable to inhibit cleavage of the nucleotide-like BNPP substrate. In support of this hypothesis, Fells *et al.* have identified compounds that competitively inhibit cleavage of LPC-like substrates (LPC, FS-3), but also do not inhibit cleavage of nucleotide substrates ([Fells et al., 2013](#)). Molecular docking studies using these

compounds identified a number of key interactions with ATX residues, including Leu214, Ala218, Phe275 and Tyr307 that correspond well with the ATX residues identified in this study ([Fells et al., 2013](#)). Further, the authors predicted that these compounds bind in the hydrophobic pocket away from the zinc ions in a similar manner to PAT-078. To test the hypothesis that competitive inhibitors require coordination with the zinc atoms in order to inhibit cleavage of nucleotide-like substrates, we rationally designed analogues of PAT-078 that would be expected to coordinate with the zinc atoms. These molecules remained competitive inhibitors of ATX, but now displayed 100% inhibition of BNPP cleavage with IC₅₀ values of ~0.01 μM (data not shown), thus supporting our hypothesis.

PAT-347 bound to an allosteric site in the enzyme is consistent with its non-competitive mode of lysoPLD inhibition. Interestingly, in this crystal structure co-crystallized with PAT-347 and was shown to be bound in the active site/hydrophobic pocket. Since LPA was not added during the crystallization process, this LPA species was selected during the insect cell culture and carried throughout the protein purification process. Others have described the presence of 14:0 phospholipids and a Ca⁺²-independent phospholipase A (PLA2) activity in Sf9 cells ([Marheineke et al., 1998](#); [Yeh et al., 1997](#)), so it is likely that the phospholipids can be converted to lysophospholipids within insect cells. The selection of the 14:0 LPA species is consistent with the identification of 14:0 LPC as a preferred ATX substrate *in vitro* ([Giganti et al., 2008](#)). The binding of LPA with the same acyl chain as the preferred LPC species suggests that the acyl chains of both likely fill similar space. Since LPA is bound in the hydrophobic pocket, any molecule that occupies similar space would prevent LPA from

binding and co-crystallizing. PAT-078, PAT-494 and PAT-352 bind fully or partially in the hydrophobic pocket, so it is not surprising that these compounds did not co-crystallize with LPA. While it is not entirely clear how allosteric compounds inhibit cleavage of LPC, one potential explanation is that allosteric binding does not affect cleavage of LPC, but it blocks the generated LPA from exiting the enzyme through the hydrophobic channel, thereby trapping it and preventing binding of a second substrate molecule. Thus, one molecule of ATX bound to an allosteric inhibitor would bind and turn over one substrate molecule prior to being inhibited. Further biochemical studies with the allosteric inhibitors will be necessary to confirm this.

From the X-ray crystal structures, it is clear that PAT-494 binds orthogonally to PAT-078 and their binding sites only partially overlap. The hydantoin and vinyl-nitrile portion of each molecule can both form a π - π -interaction with Tyr307 and both make an H-bond with the Phe275 amide. These key interactions have been reported for other inhibitors co-crystallized with rodent ATX ([Kawaguchi et al., 2013](#)). However, unlike PAT-078, PAT-494 does not fully occupy the hydrophobic pocket and this is consistent with its mixed mode of inhibition against the lysoPLD activity of human ATX. In the PAT-494 bound crystal structure, we unambiguously identified AA binding to the previously reported hydrophobic channel, which was hypothesized to be a putative second LPA-binding site (PDB ID 3NKM) ([Nishimasu et al., 2011](#)). In the mouse ATX crystal structure, this site was found to be open to solvent and was suggested to interact with the plasma membrane and facilitate channeling of LPA to its cognate receptors ([Nishimasu et al., 2011](#)). Based on our results, the hydrophobic channel which binds AA also binds PAT-347, so binding of these two molecules is mutually exclusive. This is

consistent with overlapping structural motifs on the two molecules. Both carboxylic acids are in the same region and the terminal carbon chain of AA overlaps with the indole N-substituent of PAT-347. Although PAT-352 and PAT-494 have similar binding modes, AA does not co-crystallize with PAT-352. This is the result of the backbone rearrangement that occurs upon binding of PAT-352 to site 1, which shifts a protein loop such that it occupies the same hydrophobic channel where AA would bind, thus precluding AA binding. Similarly, AA does not co-crystallize with PAT-078, likely because the carboxylic acid of PAT-078 occupies the same space as the acid in AA, again precluding AA binding. Interestingly, unlike PAT-347, AA alone does not inhibit the lysoPLD activity of ATX, while it does inhibit the ATX-mediated cleavage of FS-3. AA binding to ATX in the crystal structure occurred in the presence of PAT-494, which may indicate a stabilization of the AA binding site by the inhibitor. Thus, the inability of AA to inhibit cleavage of LPC may be related to diminished AA binding to ATX in the absence of the PAT-494 ligand. The ability of AA alone to inhibit cleavage of FS-3 may reflect binding to a distinct site on the enzyme in the absence of PAT-494, such as the hydrophobic pocket.

Like PAT-494, the structurally related PAT-352, shows a mixed mode of inhibition against the lysoPLD activity of human ATX. It is therefore not surprising that PAT-352 (site 1) binds partially in the competitive site, similarly to PAT-494, and makes very similar contacts with ATX with one major exception. PAT-352 interacts with Arg247 via coordination with both the carboxylic acid and a hydantoin carbonyl and induces a large-scale rearrangement of the 240-255 loop. As a result of this rearrangement, access to the hydrophobic pocket is restricted and a second binding site for PAT-352 is

revealed at the surface of the protein. PAT-352 and PAT-494 show similar inhibition modes and potencies with respect to the lysoPLD activity, and display similar potencies for inhibition of BNPP cleavage. However, maximum inhibition of BNPP cleavage by PAT-352 and PAT-494 is less than 100%, whereas the competitive ATX inhibitors, HA155 and PF8380, can inhibit to 100%. This partial inhibition of BNPP cleavage is consistent with these compounds binding only partially in the competitive site/hydrophobic pocket. In contrast, PAT-352 and PAT-494 show distinct inhibition profiles against the artificial substrate, FS-3. Using FS-3 as the substrate, PAT-352 is an effective inhibitor while PAT-494 shows no inhibition of FS-3 cleavage. Modeling of the FS-3/ATX structure showed that the FS-3 hydrocarbon chain occupies the hydrophobic pocket and the phosphate portion of the molecule extends into the active site ([Fells et al., 2013](#)). As a result, compounds which bind in the active site/hydrophobic pocket would be expected to inhibit cleavage of FS-3 as shown for HA155 and PF-8380. Importantly, the modeling suggests that FS-3 does not bind in the hydrophobic channel, so compounds binding here would not be expected to inhibit FS-3 cleavage. This is consistent with the data obtained for PAT-347. With respect to the difference in FS-3 cleavage between PAT-352 and PAT-494, we hypothesize that occupying the PAT-494/352 (site 1) binding site alone is insufficient to inhibit FS-3 cleavage because these compounds do not bind in the active site and do not sufficiently occupy the hydrophobic pocket. However, for PAT-352, the backbone rearrangement occludes the entrance to the hydrophobic pocket, thus preventing binding of FS-3.

The X-ray structures obtained for the four compounds described provide the structural basis for their mechanism of inhibition and may provide guidance for the

rational design of potent, selective ATX inhibitors for therapeutic benefit. In addition, the ATX inhibitors and the knowledge of the ATX-inhibitor complexes provide tools to study the *in vitro* and *in vivo* biology of ATX. This could include the binding of ATX to other proteins or membrane surfaces such as the binding of ATX to β 3 integrins, which in turn mediates platelet interactions. Of particular interest is the role of the secondary AA binding site we identified on human ATX. This may represent a second LPC binding site that facilitates LPC migration into the catalytic site or it may function as part of the LPA transfer mechanism to LPA receptors.

ACKNOWLEDGEMENTS

We are grateful to the LS-CAT beam-line staff at Argonne National Laboratory. We thank all the PharmAkea team for their contributions to the development of ATX inhibitors, and we thank Kirk Maxey, Cayman Chemical Company, for his support of this project.

AUTHOR CONTRIBUTIONS

Participated in research design: Bain, Hutchinson, Evans, Stein, Sidhu

Conducted experiments: Stein, Bain, Prodanovich, Santini, Darlington, Evans, Stelzer,
Schaub

Contributed new reagents or analytic tools: Goulet, Sidhu, Lonergan, Calderon

Performed data analysis: Bain, Stein, Goulet, Prodanovich, Santini, Darlington

Wrote or contributed to the writing of the manuscript: Bain, Stein, Hutchinson, Evans,
Sidhu

REFERENCES

- Albers HM, van Meeteren LA, Egan DA, van Tilburg EW, Moolenaar WH and Ovaas H (2010) Discovery and optimization of boronic acid based inhibitors of autotaxin. *J Med Chem* **53**(13): 4958-4967.
- Clair T, Lee HY, Liotta LA and Stracke ML (1997) Autotaxin is an exoenzyme possessing 5'-nucleotide phosphodiesterase/ATP pyrophosphatase and ATPase activities. *J Biol Chem* **272**(2): 996-1001.
- Emsley P and Cowtan K (2004) Coot: model-building tools for molecular graphics. *Acta Crystallogr D Biol Crystallogr* **60**(Pt 12 Pt 1): 2126-2132.
- Fells JI, Lee SC, Fujiwara Y, Norman DD, Lim KG, Tsukahara R, Liu J, Patil R, Miller DD, Kirby RJ, Nelson S, Seibel W, Papoian R, Parrill AL, Baker DL, Bittman R and Tigyi G (2013) Hits of a high-throughput screen identify the hydrophobic pocket of autotaxin/lysophospholipase D as an inhibitory surface. *Molecular pharmacology* **84**(3): 415-424.
- Ferguson CG, Bigman CS, Richardson RD, van Meeteren LA, Moolenaar WH and Prestwich GD (2006) Fluorogenic phospholipid substrate to detect lysophospholipase D/autotaxin activity. *Org Lett* **8**(10): 2023-2026.
- Fulkerson Z, Wu T, Sunkara M, Kooi CV, Morris AJ and Smyth SS (2011) Binding of autotaxin to integrins localizes lysophosphatidic acid production to platelets and mammalian cells. *J Biol Chem* **286**(40): 34654-34663.
- Gierse J, Thorarensen A, Beltey K, Bradshaw-Pierce E, Cortes-Burgos L, Hall T, Johnston A, Murphy M, Nemirovskiy O, Ogawa S, Pegg L, Pelc M, Prinsen M, Schnute M, Wendling J, Wene S, Weinberg R, Wittwer A, Zweifel B and

- Masferrer J (2010) A novel autotaxin inhibitor reduces lysophosphatidic acid levels in plasma and the site of inflammation. *J Pharmacol Exp Ther* **334**(1): 310-317.
- Giganti A, Rodriguez M, Fould B, Moulharat N, Coge F, Chomarat P, Galizzi JP, Valet P, Saulnier-Blache JS, Boutin JA and Ferry G (2008) Murine and human autotaxin alpha, beta, and gamma isoforms: gene organization, tissue distribution, and biochemical characterization. *J Biol Chem* **283**(12): 7776-7789.
- Gijsbers R, Aoki J, Arai H and Bollen M (2003) The hydrolysis of lysophospholipids and nucleotides by autotaxin (NPP2) involves a single catalytic site. *FEBS Lett* **538**(1-3): 60-64.
- Hashimoto T, Okudaira S, Igarashi K, Hama K, Yatomi Y and Aoki J (2012) Identification and biochemical characterization of a novel autotaxin isoform, ATXdelta, with a four-amino acid deletion. *J Biochem* **151**(1): 89-97.
- Hausmann J, Kamtekar S, Christodoulou E, Day JE, Wu T, Fulkerson Z, Albers HM, van Meeteren LA, Houben AJ, van Zeijl L, Jansen S, Andries M, Hall T, Pegg LE, Benson TE, Kasiem M, Harlos K, Kooi CW, Smyth SS, Ovaa H, Bollen M, Morris AJ, Moolenaar WH and Perrakis A (2011) Structural basis of substrate discrimination and integrin binding by autotaxin. *Nat Struct Mol Biol* **18**(2): 198-204.
- Jansen S, Callewaert N, Dewerte I, Andries M, Ceulemans H and Bollen M (2007) An essential oligomannosidic glycan chain in the catalytic domain of autotaxin, a secreted lysophospholipase-D. *J Biol Chem* **282**(15): 11084-11091.

- Kawaguchi M, Okabe T, Okudaira S, Nishimasu H, Ishitani R, Kojima H, Nureki O, Aoki J and Nagano T (2013) Screening and X-ray crystal structure-based optimization of autotaxin (ENPP2) inhibitors, using a newly developed fluorescence probe. *ACS Chem Biol* **8**(8): 1713-1721.
- Kishi Y, Okudaira S, Tanaka M, Hama K, Shida D, Kitayama J, Yamori T, Aoki J, Fujimaki T and Arai H (2006) Autotaxin is overexpressed in glioblastoma multiforme and contributes to cell motility of glioblastoma by converting lysophosphatidylcholine to lysophosphatidic acid. *J Biol Chem* **281**(25): 17492-17500.
- Kondo M, Ishizawa T, Enooku K, Tokuhara Y, Ohkawa R, Uranbileg B, Nakagawa H, Tateishi R, Yoshida H, Kokudo N, Koike K, Yatomi Y and Ikeda H (2014) Increased serum autotaxin levels in hepatocellular carcinoma patients were caused by background liver fibrosis but not by carcinoma. *Clin Chim Acta* **433**: 128-134.
- Kremer AE, Martens JJ, Kulik W, Rueff F, Kuiper EM, van Buuren HR, van Erpecum KJ, Kondrackiene J, Prieto J, Rust C, Geenes VL, Williamson C, Moolenaar WH, Beuers U and Oude Elferink RP (2010) Lysophosphatidic acid is a potential mediator of cholestatic pruritus. *Gastroenterology* **139**(3): 1008-1018, 1018 e1001.
- Marheineke K, Grunewald S, Christie W and Reilander H (1998) Lipid composition of *Spodoptera frugiperda* (Sf9) and *Trichoplusia ni* (Tn) insect cells used for baculovirus infection. *FEBS letters* **441**(1): 49-52.

- Masuda A, Nakamura K, Izutsu K, Igarashi K, Ohkawa R, Jona M, Higashi K, Yokota H, Okudaira S, Kishimoto T, Watanabe T, Koike Y, Ikeda H, Kozai Y, Kurokawa M, Aoki J and Yatomi Y (2008) Serum autotaxin measurement in haematological malignancies: a promising marker for follicular lymphoma. *Br J Haematol* **143**(1): 60-70.
- McCoy AJ, Grosse-Kunstleve RW, Adams PD, Winn MD, Storoni LC and Read RJ (2007) Phaser crystallographic software. *Journal of applied crystallography* **40**(Pt 4): 658-674.
- Nishimasu H, Okudaira S, Hama K, Mihara E, Dohmae N, Inoue A, Ishitani R, Takagi J, Aoki J and Nureki O (2011) Crystal structure of autotaxin and insight into GPCR activation by lipid mediators. *Nat Struct Mol Biol* **18**(2): 205-212.
- Otwinowski Z and Minor W (1997) [20] Processing of X-ray diffraction data collected in oscillation mode, in *Methods in Enzymology* (Charles W. Carter, Jr. ed) pp 307-326, Academic Press.
- Pradere JP, Tarnus E, Gres S, Valet P and Saulnier-Blache JS (2007) Secretion and lysophospholipase D activity of autotaxin by adipocytes are controlled by N-glycosylation and signal peptidase. *Biochim Biophys Acta* **1771**(1): 93-102.
- Shimizu Y, Murao K, Tanaka T, Kubo Y and Tokumura A (2014) Increased lysophospholipase D activity of autotaxin in sera of patients with atopic dermatitis. *J Dermatol Sci* **74**(2): 162-165.
- Sievers F, Wilm A, Dineen D, Gibson TJ, Karplus K, Li W, Lopez R, McWilliam H, Remmert M, Soding J, Thompson JD and Higgins DG (2011) Fast, scalable

generation of high-quality protein multiple sequence alignments using Clustal Omega. *Mol Syst Biol* **7**: 539.

Stefan C, Jansen S and Bollen M (2005) NPP-type ectophosphodiesterases: unity in diversity. *Trends Biochem Sci* **30**(10): 542-550.

Stracke ML, Krutzsch HC, Unsworth EJ, Arestad A, Cioce V, Schiffmann E and Liotta LA (1992) Identification, purification, and partial sequence analysis of autotaxin, a novel motility-stimulating protein. *J Biol Chem* **267**(4): 2524-2529.

Su SC, Hu X, Kenney PA, Merrill MM, Babaian KN, Zhang XY, Maity T, Yang SF, Lin X and Wood CG (2013) Autotaxin-lysophosphatidic acid signaling axis mediates tumorigenesis and development of acquired resistance to sunitinib in renal cell carcinoma. *Clin Cancer Res* **19**(23): 6461-6472.

Tanaka M, Okudaira S, Kishi Y, Ohkawa R, Iseki S, Ota M, Noji S, Yatomi Y, Aoki J and Arai H (2006) Autotaxin stabilizes blood vessels and is required for embryonic vasculature by producing lysophosphatidic acid. *J Biol Chem* **281**(35): 25822-25830.

Tokumura A, Majima E, Kariya Y, Tominaga K, Kogure K, Yasuda K and Fukuzawa K (2002) Identification of human plasma lysophospholipase D, a lysophosphatidic acid-producing enzyme, as autotaxin, a multifunctional phosphodiesterase. *J Biol Chem* **277**(42): 39436-39442.

Umezū-Goto M, Kishi Y, Taira A, Hama K, Dohmae N, Takio K, Yamori T, Mills GB, Inoue K, Aoki J and Arai H (2002) Autotaxin has lysophospholipase D activity leading to tumor cell growth and motility by lysophosphatidic acid production. *J Cell Biol* **158**(2): 227-233.

- Vagin AA, Steiner RA, Lebedev AA, Potterton L, McNicholas S, Long F and Murshudov GN (2004) REFMAC5 dictionary: organization of prior chemical knowledge and guidelines for its use. *Acta Crystallogr D Biol Crystallogr* **60**(Pt 12 Pt 1): 2184-2195.
- van Meeteren LA, Ruurs P, Christodoulou E, Goding JW, Takakusa H, Kikuchi K, Perrakis A, Nagano T and Moolenaar WH (2005) Inhibition of autotaxin by lysophosphatidic acid and sphingosine 1-phosphate. *J Biol Chem* **280**(22): 21155-21161.
- van Meeteren LA, Ruurs P, Stortelers C, Bouwman P, van Rooijen MA, Pradere JP, Pettit TR, Wakelam MJ, Saulnier-Blache JS, Mummery CL, Moolenaar WH and Jonkers J (2006) Autotaxin, a secreted lysophospholipase D, is essential for blood vessel formation during development. *Mol Cell Biol* **26**(13): 5015-5022.
- Yeh LH, Bajpai RK and Sun GY (1997) Membrane lipid metabolism and phospholipase activity in insect *Spodoptera frugiperda* 9 ovarian cells. *Lipids* **32**(5): 481-487.
- Yung YC, Stoddard NC and Chun J (2014) LPA receptor signaling: pharmacology, physiology, and pathophysiology. *Journal of lipid research* **55**(7): 1192-1214.

FOOTNOTES

Send requests for reprints to: Gretchen Bain, 12780 El Camino Real, Suite 200, San Diego CA 92130 (gbain@pharmakea.com)

Adam J. Stein and Gretchen Bain contributed equally to this work

Figure Legends

Figure 1 Overall structure of ATX. (A) Domain architecture of human autotaxin highlighting the two Somatomedin B-like (SMB) domains (SMB1 in purple and SMB2 in yellow), the catalytic domain (green), and the nuclease-like (NUC) domain (cyan). The catalytic Thr210 is highlighted in green and the glycosylation sites are highlighted in red. (B) The human ATX crystal structure depicting the domains in Figure 1A. The large dark spheres depict the active site zincs. Human ATX topology is shown, displaying the SMB1 and SMB2 domains, the NUC domain (cyan), and the catalytic domain which contains both lysoPLD and PPase/PDE activities.

Figure 2 Inhibition of ATX enzymatic activities. (A) Structures of the ATX inhibitors PAT-078, PAT-347, PAT-494, PAT-352, HA155 and PF-8380. (B) Schematic of the three ATX activity assays (LPC cleavage which represents LysoPLD activity, BNPP cleavage and FS-3 cleavage) used for screening inhibitors. (C-E) Concentration response curves for the inhibition of ATX activity as measured by the cleavage of the endogenous substrate, LPC (C) or the artificial substrates BNPP (D) and FS-3 (E).

Figure 3 Enzyme kinetics in the presence of inhibitors. (A, C, E, G) Substrate/velocity curves and alpha values for ATX lysoPLD activity in the presence of varying concentrations (0.5X-4X the IC_{50} value) of PAT-078 (A), PAT-347 (C), PAT-494 (E) and PAT-352 (G). (B, D, F, H) Plots of K_m and V_{max} values vs. inhibitor concentration for PAT-078 (B), PAT-347 (D), PAT-494 (F) and PAT-352 (H). The K_m and V_{max} values were derived from the substrate/velocity curves shown in A, C, E and G.

Figure 4 Crystal structures of human ATX bound to PAT-078 and PAT-347. (A) Crystal structure of PAT-078 (grey) showing a single hydrogen bond between the amide backbone of Phe275 and the vinyl-nitrile group of PAT-078 (dotted line). One water molecule (shown as a small red sphere) coordinates to the benzoic acid of PAT-078 (dotted line). Key amino acid residues are colored in yellow. Amino acid residues in salmon outline the hydrophobic pocket described in the text. The zinc coordination sites are shown as large spheres. (B) Overlay of PAT-078 (grey) and HA155 (green) binding to human ATX. The zinc coordination sites are shown as large spheres. Key amino acid residues are colored yellow. (C) PAT-347 (purple) binds outside the active site in the hydrophobic channel (non-competitive site) while the 14:0 LPA (orange) is bound in the active site with the acyl chain bound in the hydrophobic pocket. The zinc coordination sites are shown as large spheres. Residues His252 and Phe250 (salmon) highlight the interactions with the indole ring. (D) Overlay of LPA (orange), PAT-078 (grey) and PAT-347 (purple) binding sites. The zinc coordination sites are shown as large spheres.

Figure 5 Crystal structure of human ATX bound to PAT-494. (A) PAT-494 (salmon) bound partially in the competitive site and extending into the hydrophobic channel (non-competitive site) with arachidonic acid (yellow) bound fully in the hydrophobic channel. Key amino acid residues described in the text are shown in purple. The zinc coordination sites are shown as large spheres. (B) Overlay of the PAT-078 (grey), PAT-494 (salmon) and arachidonic acid (yellow) crystal structures. Phe275 (purple) is shown for reference. (C) Overlay of the PAT-347 (green), PAT-494 (salmon), and arachidonic acid (yellow) crystal structures. Phe275 (purple) is shown for reference. (D) A surface representation of both the LPA binding site identified in the PAT-347 crystal structure

(orange) and the arachidonic acid binding site identified in the PAT-494 crystal structure (yellow) shows no overlap between the two sites.

Figure 6 Crystal structure of human ATX bound to PAT-352. (A) Two molecules of PAT-352 (cyan) are bound. One molecule binds partially in the competitive binding site and extends into the hydrophobic channel (site 1) and a second molecule binds on the surface of ATX (site 2). The zinc coordination sites are shown as large spheres. (B) Overlay between the PAT-352 site 1 (cyan) crystal structure and the PAT-347 (green) crystal structure showing how the mobile loop (yellow) occludes the non-competitive binding site of PAT-347 (hydrophobic channel) and displaces the Arg247 residue (grey). Arg247* (yellow) indicates the displaced residue in the PAT-352 crystal structure. Arrows indicate the location of the ATX mobile loop in the absence of PAT-352 binding. (C) Close-up of the second PAT-352 binding site (site 2) showing PAT-352 (cyan) sandwiched between Arg440 (salmon), Met233 (salmon) and Phe242 (yellow) from the top and Trp254 (yellow) from the bottom. The primary PAT-352 site (site 1) with the displaced Arg247* are shown for reference. Arrows indicate the ATX mobile loop region. (D) Overlay of all human crystal structures described in this paper. PAT-078 (cyan), PAT-352 bound in site 1 and site 2 (magenta), PAT-494 (salmon) and 14:0 LPA (orange), all bind in various locations in the competitive site. PAT-347 (green) and AA (yellow) bind completely in the non-competitive site. The zinc coordination sites are shown as large spheres. (E) A native surface representation of human ATX including all regions described in the paper. (F) Same surface representation and orientation in Figure 6E with 14:0 LPA (orange) and AA (yellow) bound in their respective sites.

PDB Captions

1. 4ZG6 represents the PDB deposition code for the ATX/PAT-078 crystal structure.
2. 4ZG7 represents the PDB deposition code for the ATX/PAT-347 crystal structure.
3. 4ZGA represents the PDB deposition code for the ATX/PAT-494 crystal structure.
4. 4ZG9 represents the PDB deposition code for the ATX/PAT-352 crystal structure.

TABLE 1
 Data collection and refinement statistics

	PAT-078	PAT-352	PAT-347	PAT-494
Data collection				
Space group	P1	C222 ₁	P2 ₁	P1
Cell dimensions				
<i>a</i> , <i>b</i> , <i>c</i> (Å)	63.62, 70.49, 107.37	127.46, 209.99, 188.19	61.8, 85.8, 83.9	53.67, 64.00, 70.51
α , β , γ (°)	104.65, 99.27, 99.86	90, 90, 90	90, 111.3, 90	99.44, 108.40, 98.61
Resolution (Å)	50-1.80 (1.86-1.80)	50-2.95 (3.06-2.95)	50-1.75 (1.81-1.75)	50-2.60 (2.69-2.60)
<i>R</i> _{sym} or <i>R</i> _{merge}	0.057 (0.66)	0.157 (.810)	0.061 (0.49)	0.070 (0.39)
<i>I</i> / σ <i>I</i>	19.0 (1.6)	10.7 (2.0)	17.6 (1.9)	11.5 (1.8)
Completeness (%)	96.2 (96.0)	99.3 (99.9)	98.9 (98.1)	97.9 (97.8)
Redundancy	2.0 (2.0)	4.8 (4.9)	3.4 (3.4)	2.0 (2.0)
Mosaicity (°)	0.636	0.494	0.523	1.14
Molecules in A.U.	2	2	1	1

*Parenthesis denotes the highest resolution shell statistics.

TABLE 1 (con't)

	PAT-078	PAT-352	PAT-347	PAT-494
Refinement Statistics				
Resolution Range (Å)	20-1.80	30-2.95	20-1.75	30-2.60
R _{cryst} (%)	22.0	17.9	16.4	20.7
R _{free} (%)	26.5	24.4	19.4	27.4
Number of Molecules				
Inhibitor	2	4	1	1
Zn ⁺² /Ca ⁺² /Na ⁺¹	4/2/4	4/2/4	2/1/2	2/1/0
EDO	-	3	-	1
GOL	2	-	7	-
SCN-	12	-	-	2
Water	614	51	495	18
NAG	4	4	2	2
BMA	2	1	-	2
ARA	-	-	-	1
LPA	-	-	1	-
Bond Lengths (Å)	0.011	0.011	0.010	0.011
Bond angles (°)	1.51	1.66	1.49	1.60
Average B-factors (Å²)				
Main chain atoms	37.7	60.4	22.2	69.7
Side chain atoms	39.7	62.1	24.4	70.6
Inhibitor	48.5	58.1	18.3	59.3
Zn ⁺² /Ca ⁺² /Na ⁺¹	36.3/27.1/35.5	74.1/51.8/59.1	19.0/16.4/24.1	65.5/63.1
EDO	-	52.6	-	67.5
GOL	36.7	-	34.6	-
SCN-	51.8	-	-	77.0
Water	37.6	41.9	29.1	55.2
NAG	32.6	55.3	23.0	68.2
BMA	58.9	93.0	-	101.9
ARA	-	-	-	54.2
LPA	-	-	36.2	-
Ramachandran Plot (%)				
Favored Residues	96.6	93.4	97.4	91.7
Allowed Residues	3.2	6.2	2.6	7.2
Outlier Residues	0.2	0.4	0	1.1

TABLE 2
 Average IC₅₀ values and maximum inhibition of the various ATX enzymatic activities

Compound	LPC substrate		BNPP substrate		FS-3 substrate	
	Ave IC ₅₀ (μM) (StdDev) n	Ave Max inhib (%)	Ave IC ₅₀ (μM) (StdDev) n	Ave Max inhib (%)	Ave IC ₅₀ (μM) (StdDev) n	Ave Max inhib (%)
PAT-078	0.472 (0.146) 5	100	0.002 (0.002) 3	15	0.011 (0.009) 5	96
PAT-347	0.002 (0.0003) 3	100	0.003 (0.002) 3	57	NA 3	
PAT-494	0.020 (0.007) 3	100	0.006 (0.005) 3	51	NA 3	
PAT-352	0.026 (0.009) 6	100	0.005 (0.001) 3	74	0.0007 (0.0003) 5	78
HA155	0.182 (0.071) 3	100	0.007 (0.003) 3	100	0.002 (0.001) 5	100
PF-8380	0.005 (0.003) 3	100	0.001 (0.000) 4	100	0.0004 (0.0004) 4	100

n= number assays performed; NA = not active

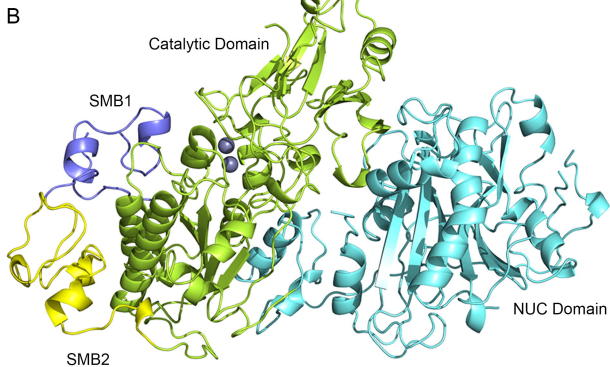
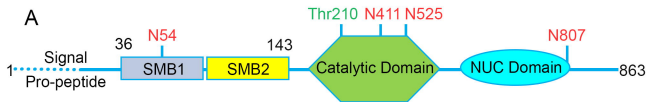


Figure 1

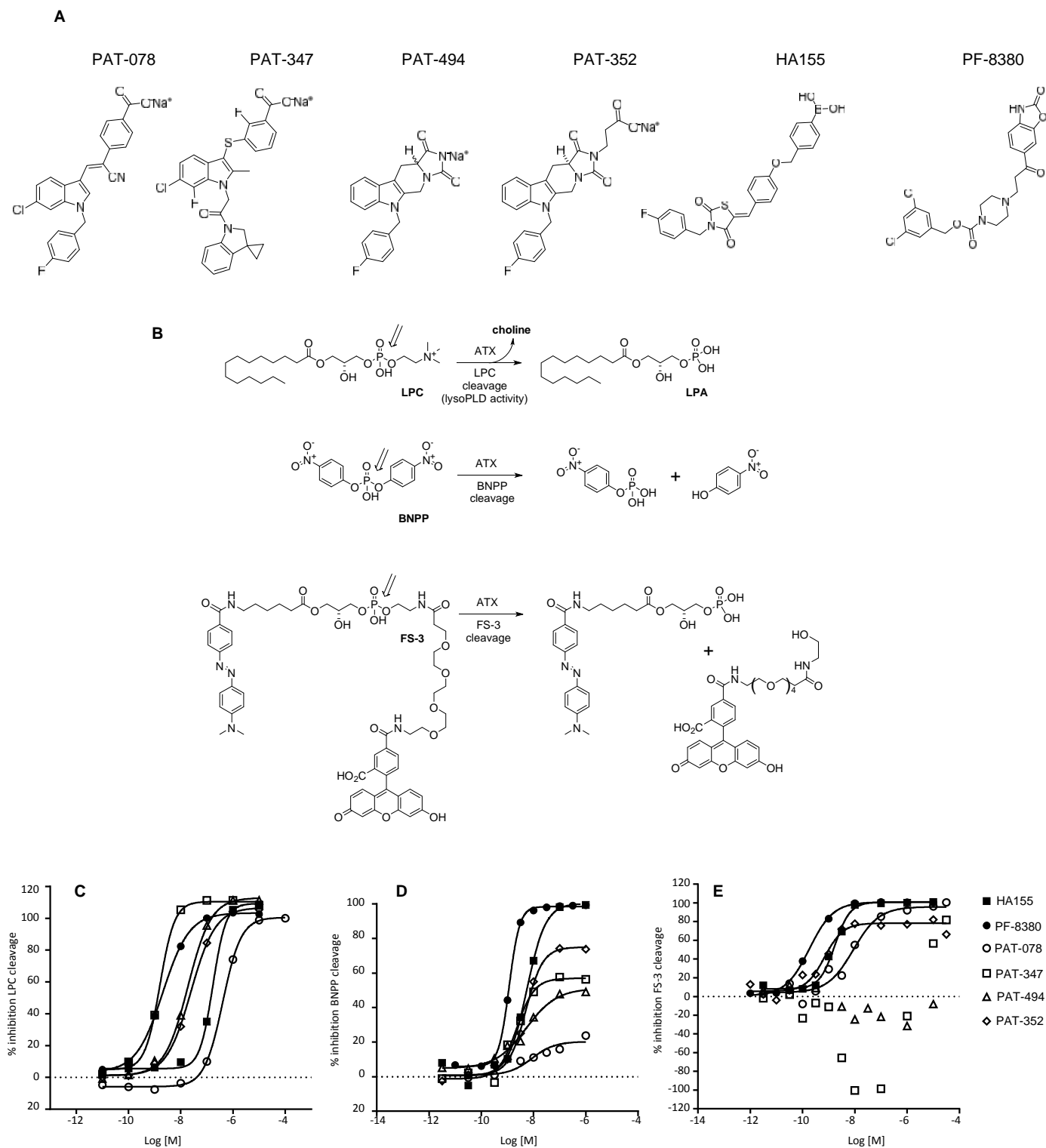
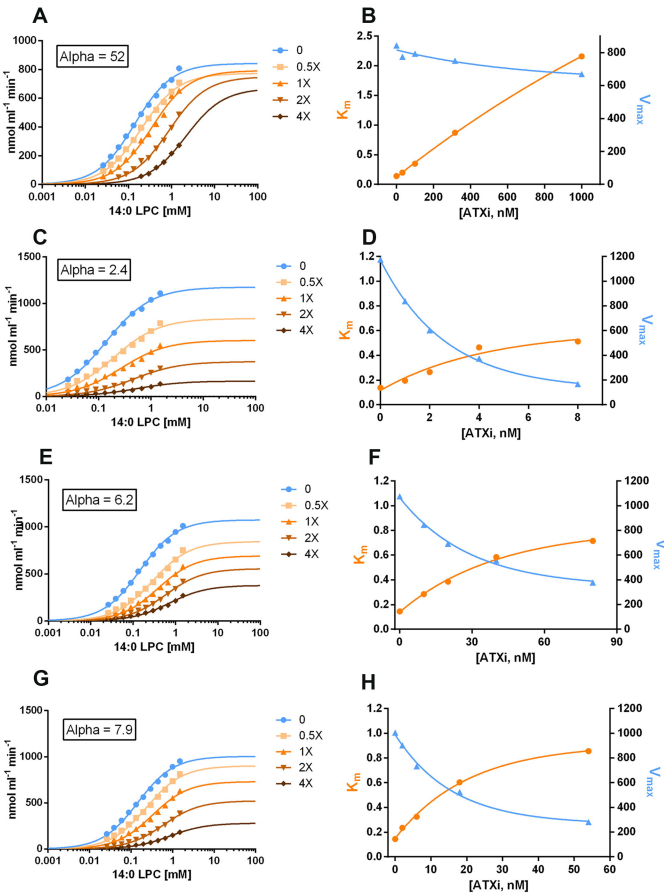


Figure 2

Figure 3



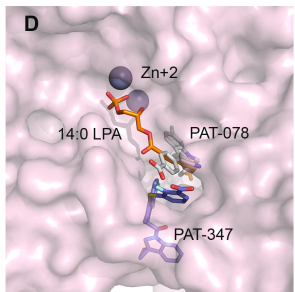
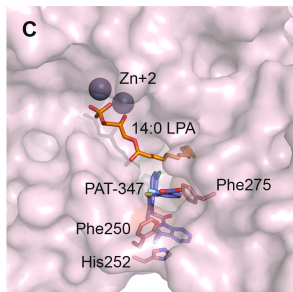
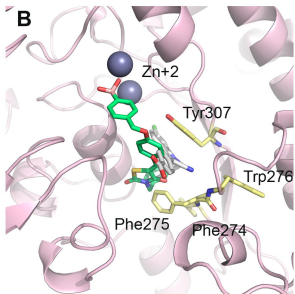
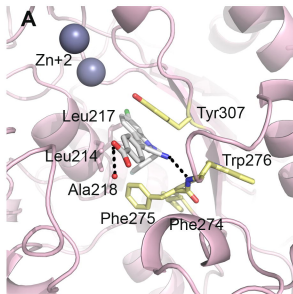


Figure 4

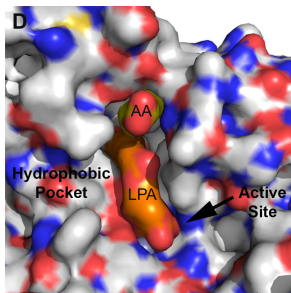
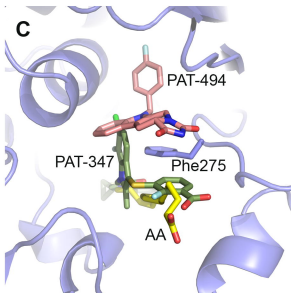
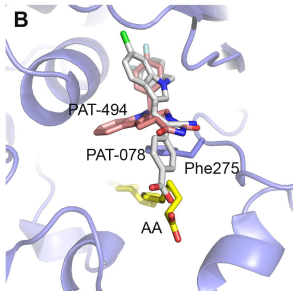
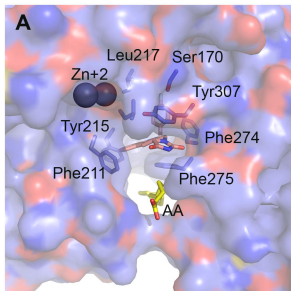


Figure 5

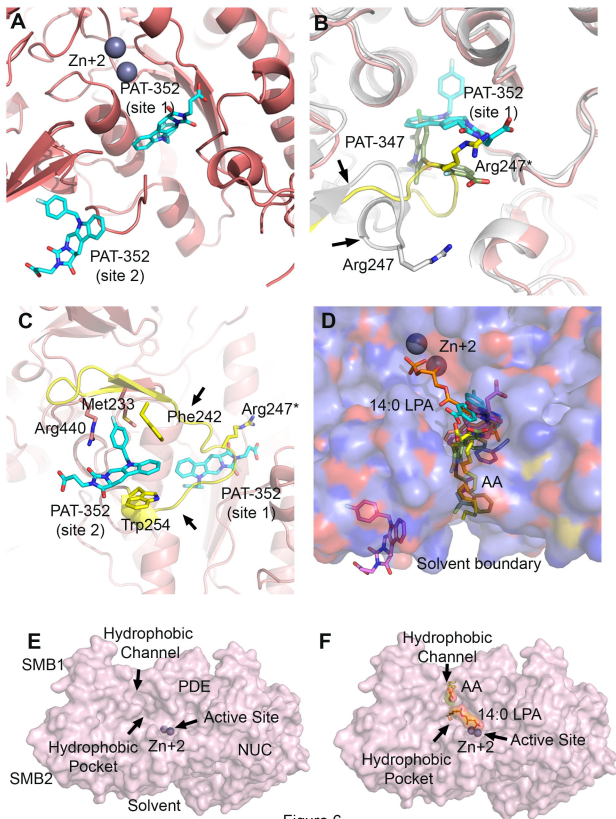


Figure 6